STAR FORMATION PROPERTIES IN BARRED GALAXIES. III. STATISTICAL STUDY OF BAR-DRIVEN SECULAR EVOLUTION USING A SAMPLE OF NEARBY BARRED SPIRALS

ZHI-MIN ZHOU[1], CHEN CAO[2,3,4], AND HONG WU[1]

[1] Key Laboratory of Optical Astronomy, National Astronomical Observatories, Chinese Academy of Sciences, Beijing 100012, China; zmzhou@bao.ac.cn, hwu@bao.ac.cn

[2] School of Space Science and Physics, Shandong University at Weihai, Weihai, Shandong 264209, China; caochen@sdu.edu.cn

[3] Shandong Provincial Key Laboratory of Optical Astronomy & Solar-Terrestrial Environment, Weihai, Shandong 264209, China

[4] Visiting Scholar, Infrared Processing and Analysis Center (IPAC), California Institute of Technology, Pasadena, CA 91125, USA

ABSTRACT

Stellar bars are important internal drivers of secular evolution in disk galaxies. Using a sample of nearby spiral galaxies with weak and strong bars, we explore the relationships between the star formation feature and stellar bars in galaxies. We find that galaxies with weak bars tend coincide with low concentrical star formation activity, while those with strong bars show a large scatter in the distribution of star formation activity. We find enhanced star formation activity in bulges toward stronger bars, although not predominantly, consistent with previous studies. Our results suggest that different stages of the secular process and many other factors may contribute to the complexity of the secular evolution. In addition, barred galaxies with intense star formation in bars tend to have active star formation in their bulges and disks, and bulges have higher star formation densities than bars and disks, indicating the evolutionary effects of bars. We then derived a possible criterion to quantify the different stages of the bar-driven physical process, while future work is needed because of the uncertainties.

Key words: galaxies: evolution – galaxies: general – galaxies: photometry – galaxies: spiral – galaxies: structure

1. INTRODUCTION

Stellar bars are ubiquitous in disk galaxies. Observed bar fractions range from one- to two-thirds in the local universe depending on the method used to identify bars and the sample and wave-bands observed (Eskridge et al. 2000; Menéndez-Delmestre et al. 2007). Bars are also found in galaxies up to $z \sim 1$ (Sheth et al. 2008; Melvin et al. 2014). Bars are one of the major internal drivers of secular evolution in galaxies (see Kormendy & Kennicutt 2004 for a review). The nonaxisymmetric gravitational potentials of bars can redistribute the angular momentum of gas and stars in galactic disks, induce large-scale streaming motions (Regan et al. 1995, 1999; Sakamoto et al. 1999b; Sheth et al. 2005), and result in an increase in gas mass and enhancement of star formation activity in the galactic central regions (Sérsic & Pastoriza 1965; Hawarden et al. 1986; Ho et al. 1997).

Many studies, both theoretical and observational, have been undertaken to explore the process of bar-driven secular evolution. Numerical simulations have established that the gravitational torque of large-scale bars can make gas lose angular momentum and allow it to move inward toward the galactic center (Athanassoula 1992; Sellwood & Wilkinson 1993; Piner et al. 1995; Athanassoula 2003). Observations indicate that barred spirals have higher molecular gas concentrations in their central kiloparsecs than unbarred systems (Sakamoto et al. 1999b; Sheth et al. 2005). Younger stellar populations and higher star formation rates (SFRs) are also found in the bulges of barred galaxies compared with unbarred ones (e.g., Sérsic & Pastoriza 1965; Huang et al. 1996; Alonso-Herrero & Knapen 2001; Kormendy & Fisher 2005; Fisher 2006; Wang 2008; Coelho & Gadotti 2011; Wang et al. 2012). Kormendy & Kennicutt (2004) showed correlations between the surface densities of SFR and gas and compared these correlations in the circumnuclear star-forming

rings in barred galaxies with those in the disks of spiral galaxies. They found that both SFR densities and gas densities in circumnuclear rings are higher than those in the outer disks.

However, some observations found conflicting results as to how a bar affects the evolution of disk galaxies. Ho et al. (1997) showed that the bars in late-type spirals have no noticeable impact on the likelihood of a galaxy for hosting nuclear star formation. Furthermore, there are some barred galaxies with no molecular gas detected in their nuclear regions where it may have been consumed by star formation (Sheth et al. 2005). Using emission-line diagnostics to identify central star formation activity in galaxies, Oh et al. (2012) found that bar effects on central star formation seem higher in redder galaxies and are more pronounced with increasing bar length, but the effects on central star formation are not visible in blue galaxies. Similarly, Wang et al. (2012) found that only strong bars result in enhanced central star formation in galaxies, but not weak bars. Ellison et al. (2011) found enhanced fiber SFR and metallicities just exist in massive barred galaxies, and no significant correlation between SFR enhancement and bar length or ellipticity. Based on the Galaxy Zoo 2 data set, Cheung et al. (2013) studied the behavior of bars in disk galaxies and found that the trends of bar likelihood and bar length with bulge prominence are bimodal with specific star formation rates (SSFRs).

In previous studies, comparisons were often made between barred and unbarred galaxies, whereas the comparisons between the variation in stellar bar properties and their associated star formation are crucial to the understanding of the bar-driven secular process in galaxies. Thus, a large sample and multi-wavelength data are required. In our previous work, three barred galaxies in different evolutionary stages were analyzed based on the data in different wavelength bands: NGC 7479 in Zhou et al. (2011, hereafter Paper I) and NGC 2903 and NGC 7080 in Zhou et al. (2012, hereafter Paper II). In this

paper, we use multi-wavelength data from the optical to the infrared (IR) to analyze a relatively large sample of nearby barred galaxies (with both weak and strong bars, including early to late Hubble types). We aim to statistically study the correlation between star formation activity and bar properties, especially its strength.

This paper is organized as follows. In Section 2, we describe the selection of the sample and give a brief introduction of the data. In Section 3, we present the method used for image decomposition and derive the structural characterization of our galaxies. We explore the correlations between the star formation and bar properties in Section 4. Then we discuss our results and explore the possible evolutionary episodes of bar-driven secular evolution in Section 5. Finally, we finish with our summary and conclusions in Section 6.

2. SAMPLE AND DATA

2.1. Sample Selection

Our sample is mainly selected from three *Spitzer* local programs: the Spitzer Infrared Nearby Galaxies Survey (SINGS; Kennicutt et al. 2003), the Local Volume Legacy (LVL; Lee 2008; Dale et al. 2009), and the Infrared Hubble Atlas (Pahre et al. 2004b). From all nearby galaxies in these programs, we selecte galaxies with bars, i.e., with Hubble type of SB and SAB. In addition, we apply an inclination cut to remove apparently edge-on galaxies (inclination $> 65°$ or ellipticity < 0.58), as well as removing objects that are obviously merging. This produces the final sample size of 50 galaxies.

Table 1 shows the general properties of the 50 galaxies in our sample (see Figure 1). The distances given in Table 1 were luminosity distances from the NASA Extragalactic Database (NED).[5] The distance of the studied sample has a mean value of 20.5 Mpc and a maximum value of 63.6 Mpc. The standard isophotal galaxy diameters (D_{25}) are $\sim 3'$, with all sizes larger than $1'$. Galaxies in the sample include a wide variety of Hubble types. There are 27 SB galaxies and 23 SAB galaxies ranging from Sa to Sm, corresponding to the numerical morphological index T = 1–9. Figure 2 shows the distribution of morphology for all sample galaxies. In the following analysis we divided galaxies into early-type ($T \leqslant 4$) and late-type ($T \geqslant 5$) spirals. Thus, there are 30 early-type spirals and 20 late-type spirals in our sample. In the right panel of Figure 2, we also plotted the distance and magnitude distribution of our sample.

2.2. Data Acquisition and Reduction

In order to investigate the properties of barred galaxies, we archived IR images from the *Spitzer Space Telescope* (Werner et al. 2004) data archive. In optical wavelength, the narrow-band Hα images from ground-based telescopes are collected and used to analyze the star formation activity in galaxies. In the following section, we provide the multi-wavelength data observation/acquisition and a brief description of data reduction. A more detailed description of data acquisition and reduction can be found in Papers I and II.

2.2.1. Optical Data

In our sample, 17 galaxies were observed with the 2.16 m telescope at Xinglong Observatory of the National Astronomical Observatories of the Chinese Academy of Sciences[6] during 2009–2010. The instrument we used was the BAO Faint Object Spectrograph and Camera (BFOSC). It had a Lick 2048 × 2048 CCD detector with a plate scale of $0.''305$ pixel^{-1} and a field of view of $\sim 10' \times 10'$. The galaxies were imaged with the broadband R filter and narrowband filters centered on the appropriate redshift Hα+[N II] $\lambda\lambda 6563, 6583$ emission lines; the former images were used to subtract the stellar continuum from the Hα+[N II] images. The exposure time was typically 600 s for R-band and 3000–3600 s for Hα-band. Detailed information about the observations is listed in Table 2.

The IRAF[7] package was used for data reduction. The reduction pipeline includes checking images, adding keywords to fits headers, subtracting overscan and bias, correcting bad pixels and flat-fielding, along with removing cosmic-rays. The flux calibration of broadband images was made using the standard stars selected from the Landolt fields (Landolt 1992) and observed with the corresponding filter on the same night. After sky subtraction, the scaled R-band images were subtracted from the aligned narrowband images to obtain continuum-free Hα+[N II] line images, and the scale factors were calculated using photometric count ratios of several (~ 5) unsaturated field stars in both filter images. The narrowband images were flux calibrated based on the scale factors of R-band images and effective transmissions of narrowband and R-band filters. Comparing the calibrated Hα and R-band images indicates that there is $\sim 6\%$ of Hα emission lost in the process of removing stellar continuum, while the contribution from [N II] to the total Hα flux is typically of the order of 10% or less (Kennicutt et al. 2008). Thus, the final images have spatial resolutions of $\sim 2''$ along with a flux uncertainty of $\sim 10\%$.

In addition to our observations, optical data in R broadband and Hα narrowband filters were gathered in other previous studies and are listed in Table 3. Images of 16 galaxies from the SINGS sample were obtained from the ancillary data of the legacy project; these galaxies were observed by the Kitt Peak National Observatory (KPNO) 2.1 m telescope and the Cerro Tololo Inter-American Observatory (CTIO) 1.5 m telescope. Images of eight galaxies from the LVL sample were obtained from the ancillary data of the LVL project as part of the precursor 11 Mpc Hα Survey (Kennicutt et al. 2008). The optical data of other sample galaxies were derived from NED. The observations, data processing, and flux calibration of the optical archival images nicely matched the counterparts of our own data.

2.2.2. IR Data

To investigate the infrared properties of our sample, we retrieved the available archived *Spitzer* near-/mid-IR data from the SINGS and LVL Program data sets, including the Infrared Array Camera (IRAC; Fazio et al. 2004) imaging data at 3.6, 4.5, 5.8, and 8.0 μm bands, as well as the Multiband Imaging Photometer for Spitzer (MIPS; Rieke et al. 2004) imaging data

---

Table 1
Basic Parameters of the Whole Sample

Galaxy (name)	R.A. (J2000.0)	Decl. (J2000.0)	Morphology (RC3)	R_{25}[a] (arcseconds)	e[b] (deg)	P.A.[c] (Mpc)	D[d]	Source[e] (ref)
NGC 0023	00:09:53.40	+25:55:26	SBa	62.68	0.35	−30	58.60	4
NGC 0266	00:49:47.80	+32:16:40	SBa	88.54	0.02	0	60.40	3
NGC 0337	00:59:50.10	−07:34:41	SBd	86.52	0.37	−50	18.30	1
NGC 1097	02:46:19.00	−30:16:30	SBb	279.98	0.32	−60	15.20	1
NGC 1512	04:03:54.30	−43:20:56	SBab	267.38	0.37	90	11.70	1
NGC 1566	04:20:00.40	−54:56:16	SABbc	249.53	0.21	60	20.60	1
NGC 2403	07:36:51.40	+65:36:09	SABcd	656.33	0.44	−53	2.47	1
NGC 2903	09:32:10.10	+21:30:04	SBd	377.68	0.52	17	11.70	2
NGC 2964	09:42:54.20	+31:50:50	SABbc	86.52	0.45	−83	21.90	3
NGC 3049	09:54:49.50	+09:16:16	SBab	65.63	0.34	22	24.70	1
NGC 3184	10:18:17.00	+41:25:28	SABcd	222.39	0.07	−45	11.40	1
NGC 3198	10:19:54.90	+45:32:59	SBc	255.34	0.61	37	12.10	1
NGC 3274	10:32:17.10	+27:40:07	SABd	64.14	0.52	−80	11.50	2
NGC 3319	10:39:09.40	+41:41:12	SBcd	184.98	0.45	37	13.50	3
NGC 3344	10:43:31.10	+24:55:20	SABbc	212.38	0.09	0	12.30	2
NGC 3351	10:43:57.70	+11:42:14	SBb	222.39	0.32	13	15.50	1
NGC 3368	10:46:45.70	+11:49:12	SABab	227.57	0.31	5	17.10	2
NGC 3486	11:00:23.90	+28:58:29	SABc	212.38	0.26	80	13.50	2
NGC 3521	11:05:48.60	−00:02:09	SABbc	328.94	0.53	−17	16.10	1
NGC 3627	11:20:15.00	+12:59:30	SABb	273.6	0.54	−7	14.80	1
NGC 4020	11:58:56.60	+30:24:44	SBd	62.68	0.55	15	14.40	2
NGC 4051	12:03:09.60	+44:31:53	SABbc	157.44	0.26	−45	12.70	4
NGC 4136	12:09:17.70	+29:55:39	SABc	119.43	0.07	0	12.30	3
NGC 4288	12:20:38.10	+46:17:33	SBdm	64.14	0.24	−50	10.00	2
NGC 4303	12:21:54.90	+04:28:25	SABbc	193.7	0.11	0	26.40	3
NGC 4314	12:22:32.00	+29:53:43	SBa	125.06	0.11	−34	17.10	3
NGC 4394	12:25:55.60	+18:12:50	SBb	108.92	0.11	−40	17.00	4
NGC 4491	12:30:57.10	+11:29:01	SBa	50.95	0.50	−32	11.40	4
NGC 4535	12:34:20.30	+08:11:52	SABc	212.38	0.29	0	31.70	4
NGC 4548	12:35:26.40	+14:29:47	SBb	161.11	0.21	−30	11.10	4
NGC 4569	12:36:49.80	+13:09:46	SABab	286.5	0.54	23	17.00	1
NGC 4579	12:37:43.50	+11:49:05	SABb	176.65	0.21	−85	25.40	1
NGC 4580	12:37:48.40	+05:22:07	SABa	62.68	0.22	−15	18.90	4
NGC 4647	12:43:32.30	+11:34:55	SABc	86.52	0.21	−55	23.90	3
NGC 4654	12:43:56.60	+13:07:36	SABcd	146.93	0.43	−52	18.80	3
NGC 4725	12:50:26.60	+25:30:03	SABab	321.46	0.29	35	20.50	1
NGC 5248	13:56:16.70	+47:14:08	SBa	184.98	0.28	−50	19.80	3
NGC 5377	13:37:32.10	+08:53:06	SBbc	111.46	0.44	45	26.80	3
NGC 5457	14:03:12.60	+54:20:57	SABcd	865.21	0.07	90	4.97	2
NGC 5713	14:40:11.50	−00:17:21	SABbc	82.63	0.11	10	29.30	1
NGC 5832	14:57:45.70	+71:40:56	SBb	111.46	0.41	45	6.43	2
NGC 6701	18:43:12.40	+60:39:12	SBa	46.46	0.15	−67	53.40	4
NGC 6946	20:34:52.30	+60:09:14	SABcd	344.45	0.15	−10	6.90	1
NGC 7080	21:30:01.90	+26:43:04	SBb	54.59	0.05	90	62.70	3
NGC 7479	23:04:56.60	+12:19:22	SBc	122.21	0.24	9	27.70	3
NGC 7552	23:16:10.80	−42:35:05	SBab	101.65	0.21	90	18.80	1
NGC 7591	23:18:16.30	+06:35:09	SBbc	58.5	0.57	−35	63.60	4
NGC 7741	23:43:54.40	+26:04:32	SBcd	130.95	0.32	−10	5.53	3
NGC 7798	23:59:25.50	+20:44:59	SBc	41.41	0.09	90	28.30	3
UGC 01249	01:47:30.60	+27:19:52	SBm	207.55	0.55	−30	0.96	2

[a] Optical radii from RC3.
[b] Ellipticity from RC3.
[c] Position angle from RC3.
[d] The luminosity distance from NED.
[e] References from which objects were selected: (1) Kennicutt et al. (2003), (2) Lee (2008), (3) Pahre et al. (2004b), (4) Sanders et al. (2003).

at 24 μm band. The IRAC images at each channel had a pixel scale of 0″.75, and spatial resolutions of ∼2″.0, which are similar to those of optical Hα images. The 24 μm MIPS images had a pixel scale of 1″.5, with an FWHM of ∼6″.0.

For those galaxies that are not from the SINGS or LVL surveys, we obtained the basic calibrated data (BCD) generated from the *Spitzer* data reduction pipeline and then mosaicked

them with the MOsaicker and Point source Extractor (MOPEX) software. The final images were produced with the same plate scales and spatial resolutions similar to the archived infrared data.

In IRAC 8.0 μm band images, the flux is mainly from the polycyclic aromatic hydrocarbon (PAH) emission and dust-continuum emission (Pahre et al. 2004a, 2004b), but there is
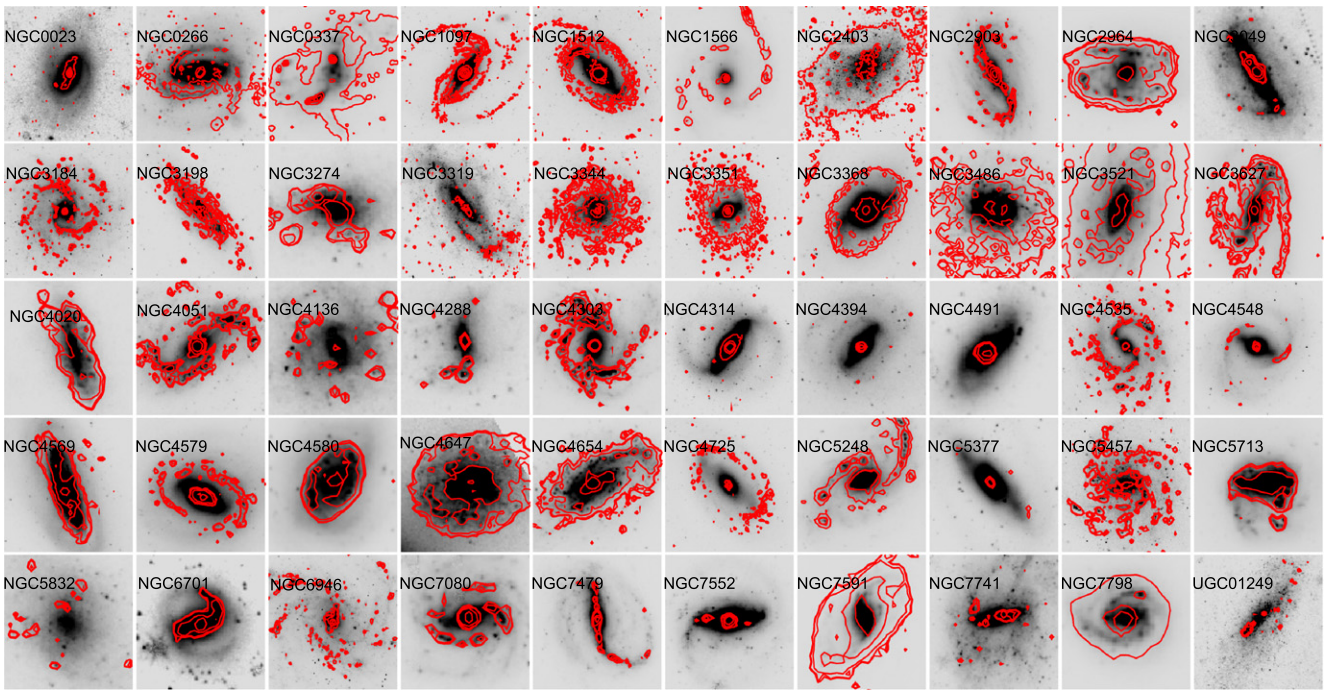
Figure 1. Mass images of the galaxies in our sample. Overplotted are the SFR imaging contours, which are in arbitrary units, optimized to show and identify the structures of the star formation complexes. The galaxy names are specified in the panels and north is up and east is to the left.
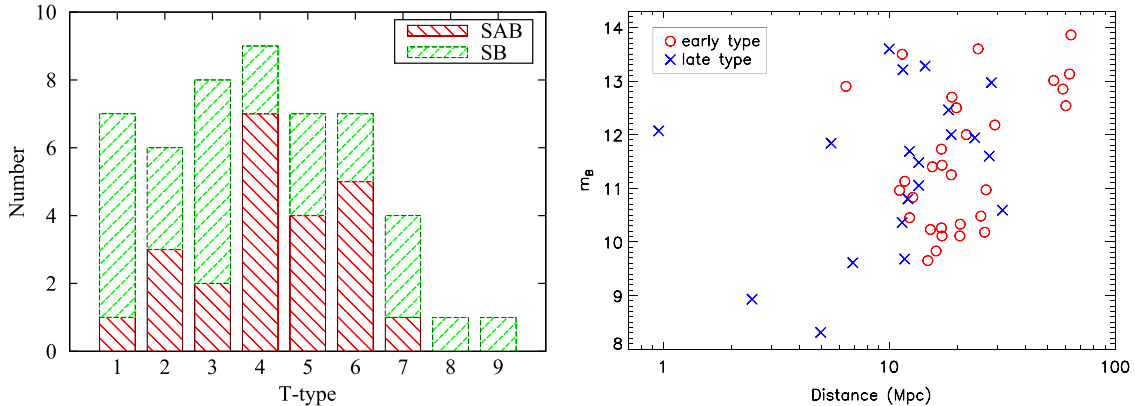

Figure 2. Morphological distribution (left) and magnitude–distance distribution (right) of our sample. In the left panel, the morphological parameter T = 1–9 corresponds to the Hubble types Sa–Sm, and the sample is divided into SB and SAB galaxies. In the right panel, the distance used is luminosity distance from NED, and the sample is divided into early (T = 1–4) and late (T = 5–9) types with red circles for early-type galaxies and blue crosses for late-type ones.

also a contribution of stellar continuum in this band. To remove the stellar contribution, the scaled IRAC 3.6 μm band images were used as the stellar continuum with a scale factor of 0.232 (Helou et al. 2004) and were subtracted from 8.0 μm images. Hereafter we referred to the continuum-free 8 μm dust emission as to 8 μm (dust).

3. IMAGE DECOMPOSITION AND BAR CHARACTERIZATION

We derive the structural parameters of bars, i.e., the length, ellipticity, and strength, with structural decomposition of barred galaxies. The IRAC 3.6 μm images, wherein the light is mainly coming from M and K giants (Sheth et al. 2010), nicely trace the stellar mass distribution in nearby galaxies although there is contamination from the 3.3 μm PAH, hot dust, and intermediate-age stars (Meidt et al. 2012). Therefore, we used the

image-fitting code BUDDA v2.2 (de Souza et al. 2004; Gadotti 2008) to perform a two-dimensional (2D) decomposition of 3.6 μm images in bar/bulge/disk stellar components. The present version of BUDDA allows us to decompose a galaxy into an exponential disk, a bulge with a Sérsic profile, and a bar (e.g., Kim et al. 2014). In the decomposition results, we obtain the galaxy structural parameters, such as the size, ellipticity, and position angle (P.A.) of each structure, which were also used to define the regions of the bulge, bar, and disk in one galaxy.

The structural parameters we obtain may be affected by inclination effects. To derive the intrinsic physical parameters, we make the corrections for the apparent values following the method of Martin (1995). In Martin (1995), the galaxy inclination i was defined using the axial ratio of the isophote 25 mag arcsec^{-2} in the B-band obtained from the Third

Table 2
XingLong 2.16 m Telescope Observations

Name	Obs. Date	Exposure Time (Section) Hα	R	Hα Filter λ/Δλ	Seeing (arcseconds)
(1)	(2)	(3)	(4)	(5)	(6)
NGC 0023	2006-09-22	2400	400	6660/70	2.0
NGC 0266	2008-01-10	3600	600	6660/70	2.7
NGC 2903	2009-12-22	3600	600	6562/70	1.7
NGC 2964	2009-01-18	2400	600	6610/70	2.0
NGC 3319	2007-03-17	3600	600	6562/70	1.9
NGC 4303	2007-02-24	1800	600	6610/70	2.6
NGC 4491	2009-04-21	3600	600	6562/70	2.3
NGC 4580	2009-04-21	3600	600	6610/70	2.3
NGC 4647	2009-01-18	1800	600	6610/70	2.0
NGC 4654	2008-02-14	3600	600	6562/70	2.1
NGC 5377	2008-02-12	3000	600	6610/70	3.0
NGC 5383	2009-04-21	1800	600	6610/70	1.8
NGC 6701	2006-07-22	2400	400	6660/70	2.6
NGC 7080	2006-09-23	2400	400	6660/70	1.8
NGC 7479	2009-09-12	3000	600	6610/70	1.8
NGC 7591	2006-09-22	3600	400	6660/70	2.4
NGC 7798	2006-08-21	2400	600	6610/70	2.7

Notes. Col. (1): name of the galaxy. Col. (2): the date of the observation. Cols. (3) and (4): exposure time in each filter in units of seconds. Col. (5): filter used for the Hα line, where λ/Δλ is the central wavelength and filter width in Å. Col. (6): seeing in arcseconds as measured on the reduced images.

Reference Catalog of Bright Galaxies (RC3; de Vaucouleurs et al. 1991) and the assumption that the galaxy is intrinsically axisymmetric at large radii. Given that the bars are thin 2D structures, the intrinsic axial ratio $(b/a)_{\rm bar}$ and length $r_{\rm bar}$ (the semimajor axis) of bars were calculated with the galaxy inclination and angles between the axes and line of nodes. Figure 3 compares the bar properties before and after correction. There is a large correction on the axial ratio of bars, but there is excellent consistency between the lengths of bars.

Figure 4 shows the distribution of the intrinsic bar lengths of the sample, both absolute and normalized. The latter is relative to the galaxy size R_{25}, which is measured by the semimajor axis of the isophote from RC3 at a brightness of 25 mag arcsec^{-2} in the B-band . The mean length of stellar bars is 5.2 kpc and 0.37 R_{25} in early types and 2.2 kpc and 0.23 R_{25} in late types, consistent with values in earlier studies (Erwin 2005; Menéndez-Delmestre et al. 2007).

Bar strength represents the ability to drive gas into the galactic center and is usually estimated using the structural parameters of the bar such as ellipticity and length of the bar (e.g., Jogee et al. 2004; Laurikainen et al. 2007). A more direct parameter is the gravitational torque Q_g, which is the maximum relative tangential force in the bar region, normalized to the underlying mean axisymmetric force field (Buta & Block 2001). Here, another bar strength parameter is used and is defined as follows Abraham & Merrifield (2000):

$$f_{\rm bar} = \frac{2}{\pi}\left[\arctan{(b/a)_{\rm bar}^{-1/2}} - \arctan{(b/a)_{\rm bar}^{+1/2}}\right], \quad (1)$$

where $(b/a)_{\rm bar}$ is the intrinsic axial ratio of the bar. The ellipticity-based parameter $f_{\rm bar}$ has been used in many previous studies (e.g., Whyte et al. 2002; Aguerri et al. 2009) and has

proved to be well correlated with Q_g (Buta et al. 2004; Laurikainen et al. 2007). The right panel of Figure 4 shows the distribution of the bar strength $f_{\rm bar}$. Bars in early-type galaxies are clearly stronger than those in late-type galaxies. Besides the parameter $f_{\rm bar}$ and bar torque, the normalized bar size $r_{\rm bar}/r_{\rm gal}$ and the combination of bar ellipticity and boxiness $\epsilon \times c$ were also used in Gadotti (2011) to estimate bar strength. We compare the two parameters with $f_{\rm bar}$ in Figure 5. This figure shows that $f_{\rm bar}$ is consistent with the other two parameters, especially $\epsilon \times c$, so it is used as the estimation of bar strength in the following analysis. Their values are also listed in Table 4.

4. RELATION BETWEEN GALACTIC STAR FORMATION PROPERTIES AND BARS

Star formation activity is an important feature in our galaxies. In our data of the sample, the Hα emission from ground-based observations and the 8 μm (dust) and 24 μm emission from *Spitzer* observations can be used as star formation tracers (Kennicutt 1998; Wu et al. 2005; Calzetti et al. 2007; Zhu et al. 2008; Kennicutt et al. 2009; Hao et al. 2011). To derive the extinction-corrected SFR distribution, we used a combination of Hα and 8 μm (dust) emissions, the former measuring the ionization rate and the latter tracing the dust-obscured component of the star formation. The calibration for the composite indicators follows the form in Zhu et al. (2008):

$$\begin{aligned} &{\rm SFR}_{H\alpha+8\,\mu m}\left(M_{\odot}\ {\rm yr}^{-1}\right) \\ &= 7.9 \times 10^{-42}\left[L(H\alpha)_{\rm obs} + 0.010L(8)\right]\left({\rm erg\ s}^{-1}\right), \quad (2) \end{aligned}$$

which adopts the Salpeter (1955) initial mass function (IMF) with a slope of 2.35 for stellar masses in the range 0.1–100 $M_{\odot}$.

In addition to the star formation activity, we also paid attention to the stellar mass of galaxies to derive the stellar properties. Here, the IRAC 3.6 μm emission is used as a proxy of the stellar mass since its light is dominated by the photospheric emission from low-mass stars as mentioned above (Smith et al. 2007; Hancock et al. 2007; Wu et al. 2007; Li et al. 2007). The calibration is from Zhu et al. (2010; their Equation (2)):

$$\begin{aligned} {\rm Log}_{10}\, M\left(M_{\odot}\right) &= (-0.79 \pm 0.03) + (1.19 \pm 0.01) \\ &\times {\rm Log}_{10}\, \nu L_{\nu}\left[3.6\,\mu m\right]\left(L_{\odot}\right), \quad (3) \end{aligned}$$

which has proved to be a good stellar mass tracer compared with K_s-band luminosity. Using these Equations, we explored the correlation between the star formation activity and stellar bars in our galaxies.

4.1. Star Formation and Stellar Mass Distribution

In order to describe the global properties of the galaxies, we first obtained the mass images and SFR images by combining the relevant images based on Equations (3) and (2), respectively. All images are listed in Figure 1, along with the distributions of stellar mass and star formation shown. Then we calculated the rotational asymmetry and concentration index of the mass and SFR images to quantify their distributions. The asymmetry describes how symmetric a galaxy system is and the concentration parameter measures how compact the light distribution is. Both indices are used to describe galaxy

Table 3
Details of the Archival Hα Images Obtained For Our Sample Galaxies

Name	Obs. Date	Telescope[a]	Exposure Time (Section) Hα	R	Seeing (arcseconds)	Source
(1)	(2)	(3)	(4)	(5)	(6)	(7)
NGC 0337	2001-10-19	CTIO1.5 m	1800	540	1.5	SINGS
NGC 1097	2001-10-17	CTIO1.5 m	1800	480	1.1	SINGS
NGC 1512	2001-10-18	CTIO1.5 m	1800	450	1.2	SINGS
NGC 1566	2001-10-21	CTIO1.5 m	1800	540	1.3	SINGS
NGC 2403	2001-11-15	KPNO2.1 m	1800	540	1.1	SINGS
NGC 3049	2002-04-11	KPNO2.1 m	1800	420	1.0	SINGS
NGC 3184	2002-04-15	KPNO2.1 m	1800	840	1.3	SINGS
NGC 3198	2002-03-09	KPNO2.1 m	1800	420	2.3	SINGS
NGC 3274	2001-03-03	Bok	1000	200	1.6	LVL
NGC 3344	2001-05-27	Bok	1000	200	1.3	LVL
NGC 3351	2001-03-29	KPNO2.1 m	1800	360	1.1	SINGS
NGC 3368	2003-04-29	VATT	1200	120	1.5	LVL
NGC 3486	2001-05-27	Bok	600	120	1.4	LVL
NGC 3521	2002-03-10	KPNO2.1 m	1800	120	1.1	SINGS
NGC 3627	2002-04-14	KPNO2.1 m	1800	840	1.1	SINGS
NGC 4020	2001-03-03	Bok	1000	200	1.4	LVL
NGC 4051	2000-03-31	JKT	3600	600	1.5	NED
NGC 4136	2001-05-16	JKT	3600	300	1.0	NED
NGC 4288	2001-05-01	Bok	1000	200	1.3	LVL
NGC 4314	1996-02-13	INT	1200	900	1.3	NED
NGC 4394	2001-02-17	JKT	3600	300	1.0	NED
NGC 4535	2000-03-06	JKT	3600	900	1.9	NED
NGC 4548	2000-03-31	JKT	3600	600	1.7	NED
NGC 4569	1988-03-25	KPNO0.9 m	3000	150	2.0	NED
NGC 4579	2002-03-10	KPNO2.1 m	1800	420	1.0	SINGS
NGC 4725	2002-03-11	KPNO2.1 m	1800	840	1.6	SINGS
NGC 5248	2001-04-11	JKT	3600	1800	1.4	NED
NGC 5457	1995-05-20	KPNO Schmidt	11700	9545	2.0	NED
NGC 5713	2001-03-30	KPNO2.1 m	1800	420	1.5	SINGS
NGC 5832	2002-03-05	Bok	1000	200	2.1	LVL
NGC 6946	2001-03-31	KPNO2.1 m	1800	420	2.1	SINGS
NGC 7552	2001-10-17	CTIO1.5 m	1800	450	1.1	SINGS
NGC 7741	2000-11-10	JKT	4800	600	1.5	NED
UGC 01249	2001-11-08	Bok	1000	200	1.7	LVL

Notes. Col. (1): name of the galaxy. Col. (2): the date of the observation. Col. (3): the telescope used. Bok means the Steward Observatory Bok 2.3 m telescope on Kitt Peak; CTIO1.5 m means Cerro Tololo Inter-American Observatory 1.5 m telescope; INT means the 2.5 m Isaac Newton Telescope on La Palma; JKT means the 1 m Jacobus Kapteyn Telescope on La Palma; KPNO0.9 m means the Kitt Peak National Observatory 0.9 m telescope; KPNO2.1 m means the Kitt Peak National Observatory 2.1 m telescope; KPNO Schmidt means the Kitt Peak National Observatory Schmidt telescope; VATT means the Lennon 1.8 m Vatican Advanced Technology Telescope on Mt. Graham, AZ. Cols. (4) and (5): exposure time in each filter in units of seconds. Col. (6): seeing in arcseconds as measured on the reduced images. Col. (7): the sources where the data are archived. LVL: Dale et al. (2009), also part of Kennicutt et al. (2008). SINGS: Kennicutt et al. (2003). NED: the NASA Extragalactic Database (of which NGC 4051, NGC 4314, NGC 4535, NGC 4548, NGC 5248, and NGC 7741 are from Knapen et al. 2004, NGC 4136 and NGC 4394 are from James et al. 2004, NGC 4569 is from Koopmann 2001, and NGC 5457 is from Hoopes et al. 2001).

morphology in many studies (e.g., Bershady et al. 2000; Conselice et al. 2000; Abraham et al. 2003; Gil de Paz et al. 2007; Muñoz-Mateos et al. 2009). The former is calculated by comparing the original image of a galaxy with its rotated counterpart (the usual rotation angle is 180°). Here, we followed the method in Conselice et al. (2000):

$$A = \frac{\sum \left| I_{180°} - I_0 \right|}{2\sum \left| I_0 \right|}, \tag{4}$$

where I_0 is the intensity distribution in the original image and $I_{180°}$ is the intensity distribution in the rotated image with a rotation angle of 180°.

The concentration index is usually calculated by the ratio of two radii containing fixed fractions of the total flux in a galaxy.

We adopt the index C_{42} defined by Kent (1985):

$$C_{42} = 5 \log_{10}\left(r_{80}/r_{20}\right), \tag{5}$$

where r_{80} and r_{20} are the semimajor axes of the ellipses containing 80% and 20% of the total luminosity, respectively. The resulting structural indices for the distributions of star formation and stellar mass in galaxies are listed in Table 4.

In Figure 6, we presented the results as a function of the bar strength f_{bar}. The early- and late-type galaxies cover approximately the same range in f_{bar}, while they have different distributions in morphological parameter spaces. To determine the correlation between two variables, we perform Spearman's rho tests and the correlation coefficients for these are listed in each panel. The right panels of Figure 6 show the correlations between the stellar mass distribution and bar strength. In the whole sample, there are no clear trends between the
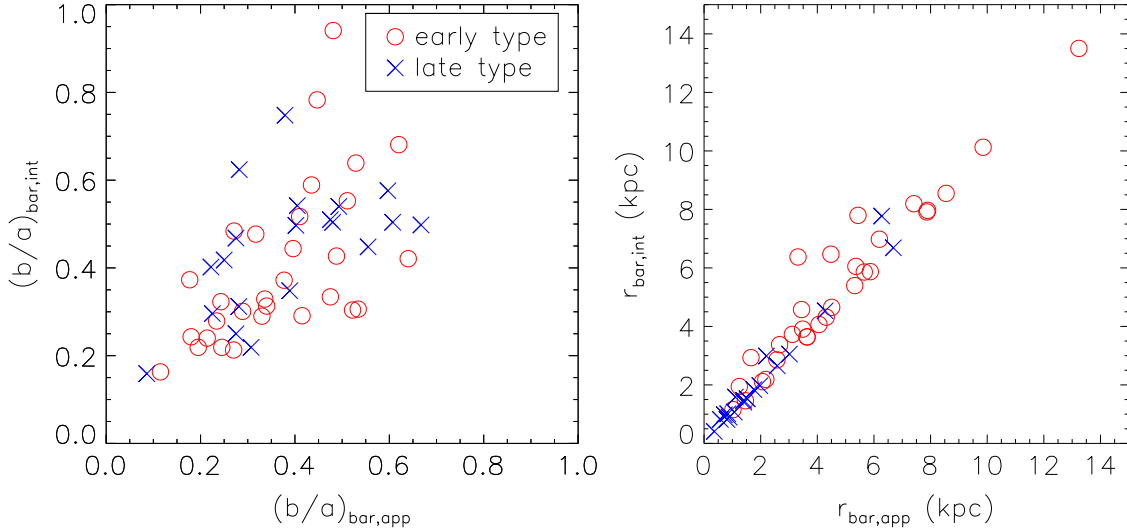
Figure 3. Comparison of bar properties between intrinsic and apparent values. The intrinsic axial ratio $(b/a)_{bar,int}$ (left) and length $r_{bar,int}$ (right) of bars were calculated with the galaxy inclination and angles between the axes and line of nodes.
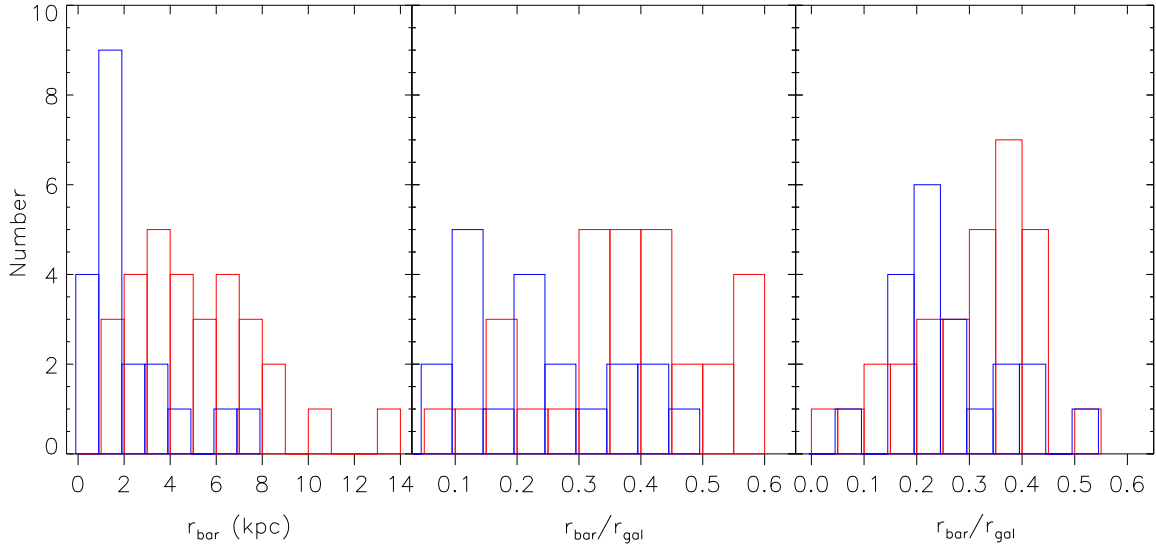

Figure 4. Distributions of bar properties of early- (red line) and late- (blue line) type spirals in our sample. The bar length (left) is indicated by the physical length of the bar semimajor axis, the normalized value (middle) is indicated by the ratio between the physical length of the bar semimajor axis and the galaxy radii at 25 mag arcsec^{-2}, and the bar strength (right) is indicated by the ellipticity-based f_{bar} parameter defined by Abraham & Merrifield (2000). In each panel, two histograms are slightly offset in the x-axis for purposes of clarity.

morphological parameters (A_{mass} and $C_{42,mass}$) and bar strength f_{bar} (Spearman's rho $r_A = -0.00$ and 0.30, respectively). However, early-type galaxies show a higher concentration index and lower asymmetry than late-type ones, which was also found by previous studies (e.g., Muñoz-Mateos et al. 2009). The results presented here show a downsizing signature of the formation of galactic structures (Cowie et al. 1996; Bundy 2006; Sheth et al. 2008), i.e., more concentrated galaxies mean more mature systems.

The left panels of Figure 6 present the variation in the distribution of star formation activity with bar strength. No clear trend is found between them (Spearman's rho $r_A = -0.12$ and 0.30, respectively). In general, star formation activity in early-type galaxies is less asymmetric and more concentrated than in late-type samples, although it is not always well

distinguished. There are tens of early-type galaxies that also have A_{SFR} or C_{SFR} similar to those of late-type ones, and most early-type galaxies with high C_{SFR} are located in the high end of the bar strength. In addition, weaker bars have lower concentric star formation activity in all types of galaxies, while the star formation activity in the spirals with stronger bars does not always have a high concentric distribution, especially in early-type galaxies. This indicates that galaxies with similar bars can have differing distributions of star formation activities.

4.2. Global Star Formation and Star Formation in Different Structural Components

In order to further explore the possible relation between star formation activity and stellar bars, we investigate the correlation between f_{bar} and SFRs, SFR surface densities (Σ_{SFR}), and
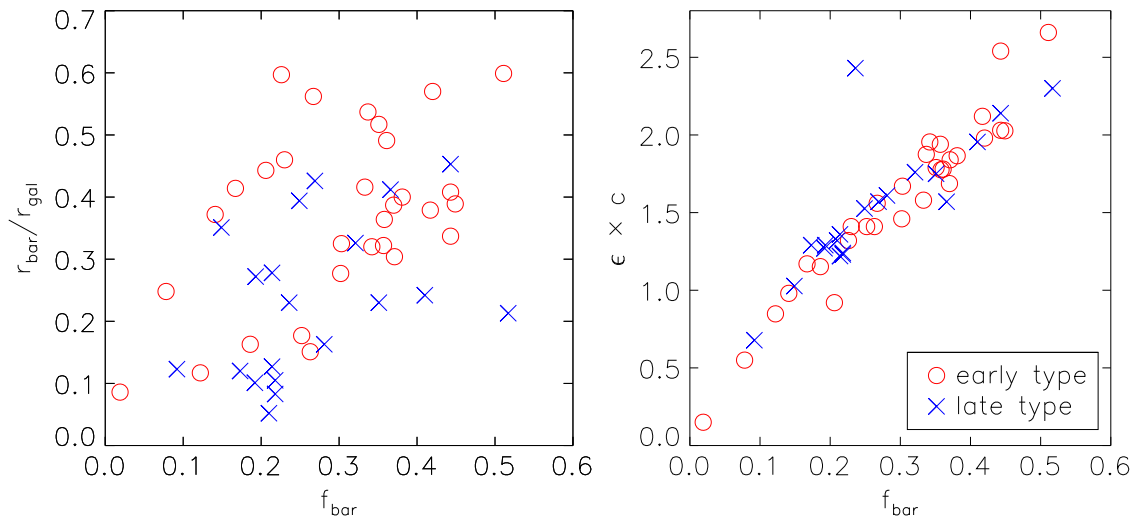
Figure 5. Comparisons between the bar strength parameter f_{bar} and two other indicators of bar strength: the normalized bar size r_{bar}/r_{gal} (left) and combination of bar ellipticity and boxiness $\epsilon \times c$ (right). The symbols are the same as in the right panel of Figure 2.

SSFRs in different galactic structural components including bulges, bars, and global galaxies. The regions of these structures are defined based on the decomposition results of the 3.6 μm images (see Section 3). Each galaxy is divided into three structural components: bulge, bar, and outer disk. In one galaxy, three structures have no overlap regions, i.e., the outer disk region is obtained by subtracting the bar and bulge field in the galaxy, and the bar region is obtained by subtracting its central bulge field. The bulge regions are defined following the decomposition results or the galactic central kiloparsec regions if no bulges exist in the decomposition fitting. The inclination i of galaxies can lead to underestimating the projected area of each galactic structure, and may affect the estimate of Σ_{SFR} (SFR/area). Therefore, we correcte this variation included by the inclination using the method in Martin (1995; see Section 3), and then calculate Σ_{SFR}. The results are listed in Table 4, and are plotted in Figure 7.

First, the top panel of Figure 7 shows the SFRs as a function of the bar strength f_{bar}. There are no clear trends for the SFRs in each structure with bar strength, although weak trends are found where the SFRs in bulges increase toward higher bar strength along with large scatter (Spearman's rho $r_A = 0.29$), similar to the result in Ellison et al. (2011). Another finding is that the early- and late-type galaxies have different behaviors in the plot: (1) early-type galaxies have higher SFRs in each regions on average and (2) late-type ones vary more in their star formation properties, especially for intermediate-strength bars ($f_{bar} \sim 0.2$–0.4). This may indicate that star formation is not a simple function of bar strength or bar-related factors, and it likely also depends on other factors (Sheth et al. 2002).

Next, we compare the SFR densities and bar strength in the middle panel of Figure 7. Similar to SFRs, the correlation coefficients are less than 0.2, indicating no clear trend of Σ_{SFR} with f_{bar}. In addition, there is no significant difference between early- and late-type galaxies in the distribution of Σ_{SFR}. This suggests that galaxies of both types have similar Σ_{SFR}, although their SFRs are different.

Last, we show the correlation between SSFR and bar strength in the bottom panel of Figure 7. There is a remarkable difference between the two types of galaxies: most late-type

samples have SSFRs higher than $0.1\,\mathrm{Gyr}^{-1}$, while most early-type ones have SSFRs lower than $0.1\,\mathrm{Gyr}^{-1}$. This trend is remarkable in all regions except for bulges. Bulges have the largest scatter in the distribution of SSFRs; the highest SSFR is $\sim 10\,\mathrm{Gyr}^{-1}$ in one late-type galaxy (NGC 4654), while the lowest value is nearly four orders of magnitude lower than it.

5. DISCUSSION

A series of analyses has been provided in this work to explore the correlations between stellar bars and star formation activities in galaxies, both sub-structures and galaxies as a whole. The analysis of these correlations constrains the effect of galactic bars to star formation and reveals secular evolution to be a complex process in barred galaxies rather than a simple one as previously assumed. In this section, we aim to discuss the possible reasons for star formation activity varying along stellar bars. Specifically, we determine how the behaviors connect to possible episodes of a bar-driven secular process.

5.1. The Impact of Bars on Star Formation Activity

For barred galaxies in our sample, we had expected some evidence for enhanced star formation activity toward stronger bars. However, we find that there are no clear trends for the star formation properties with bar strength, except for a weak dependence on the bars for SFRs and Σ_{SFR} in the bulges and global galaxies. Some previous studies also derived similar results. Using a control sample of disk galaxies, Ellison et al. (2011) compared SFRs between barred and unbarred galaxies and found that there is no correlation between bar length or bar axial ratio and the enhancement of the SFR. Some earlier studies using far-infrared emission as a proxy for SFR also did not find definite evidence that stronger bars could result in higher SFRs (e.g., Pompea & Rieke 1990; Isobe & Feigelson 1992; Roussel et al. 2001).

On the other hand, simulations indeed show that gas inflows driven by bars can enhance star formation activity in galactic central regions (e.g., Athanassoula et al. 2009). Gas being transported to the center by bars is also found in observations

Table 4
Structural and Star Formation Properties of the Sample

Name (1)	f_{bar} (2)	$C_{42,SFR}$ (3)	A_{SFR} (4)	$C_{42,mass}$ (5)	A_{mass} (6)	Log SFR ($M_\odot$ yr^{-1}) Global (7)	Bulge (8)	Bar (9)	Log Σ_{SFR}($M_\odot$ yr^{-1} kpc^{-2}) Global (10)	Bulge (11)	Bar (12)	Log SSFR (Gyr^{-1}) Global (13)	Bulge (14)	Bar (15)	Stage (16)
NGC 0023	0.23	3.62	0.31	4.33	0.06	1.06	0.79	0.58	−1.91	−0.17	−1.35	−1.08	−0.90	−0.95	c
NGC 0266	0.34	1.92	0.71	4.40	0.08	0.62	−0.64	−0.08	−2.67	−1.50	−2.34	−1.72	−2.00	−1.88	b
NGC 0337	0.25	2.43	0.54	2.58	0.21	0.20	−1.10	−0.39	−2.06	−1.00	−1.46	−0.66	−0.57	−0.61	b
NGC 1097	0.38	5.50	0.28	5.38	0.11	0.58	0.23	−0.26	−2.54	−0.53	−1.98	−1.39	−1.15	−1.45	d
NGC 1512	0.37	5.15	0.62	4.38	0.07	−0.22	−0.92	−1.27	−3.08	−0.91	−2.53	−1.34	−1.03	−1.67	d
NGC 1566	0.26	2.27	0.51	3.88	0.11	0.83	−0.64	−0.35	−2.45	−0.57	−1.60	−1.21	−1.34	−1.47	c
NGC 2403	0.22	1.89	0.47	3.37	0.25	0.24	−1.90	−0.88	−2.04	−0.68	−0.87	−0.09	−0.03	−0.05	b
NGC 2903	0.52	3.49	0.42	3.18	0.10	0.59	−0.54	−0.18	−2.56	−0.11	−1.17	−1.29	−0.81	−1.03	c
NGC 2964	0.36	2.50	0.32	3.16	0.12	0.59	−0.41	−0.25	−1.82	0.06	−1.15	−0.77	−0.54	−0.75	c
NGC 3049	0.51	4.16	0.57	4.06	0.13	−0.05	−0.27	−0.68	−2.33	−0.40	−1.67	−0.74	0.07	−0.65	c
NGC 3184	0.17	1.57	0.61	2.45	0.15	0.06	−1.57	−1.63	−2.62	−1.06	−2.19	−1.16	−0.74	−1.36	c
NGC 3198	0.09	2.02	0.46	2.79	0.11	−0.00	−1.46	−1.17	−2.85	−0.66	−2.06	−1.00	−0.63	−1.09	c
NGC 3274	0.21	1.18	0.56	2.75	0.12	−0.85	−1.89	−1.64	−2.44	−1.17	−1.76	−0.38	−0.21	−0.38	b
NGC 3319	0.28	2.34	0.74	3.16	0.09	−0.69	−3.70	−1.68	−3.36	−2.35	−2.37	−1.05	−1.24	−0.99	b
NGC 3344	0.12	2.30	0.72	2.96	0.11	0.18	−1.53	−1.37	−2.51	−0.27	−2.03	−1.03	−0.76	−1.57	d
NGC 3351	0.37	5.86	0.30	4.60	0.05	0.52	−0.03	−0.54	−2.42	−0.71	−2.07	−1.23	−1.01	−1.45	d
NGC 3368	0.33	3.33	0.41	4.55	0.05	0.32	−0.47	−0.14	−2.72	−1.17	−1.91	−1.73	−1.75	−1.64	b
NGC 3486	0.19	2.50	0.59	4.00	0.11	0.04	−2.25	−1.45	−2.74	−1.65	−1.95	−0.99	−1.83	−1.41	b
NGC 3521	0.02	2.24	0.29	3.70	0.07	1.02	−1.12	−0.06	−2.29	−0.78	−1.19	−1.26	−1.87	−1.40	b
NGC 3627	0.30	2.62	0.63	3.50	0.16	1.07	−0.57	0.15	−2.00	−0.76	−1.37	−1.06	−1.43	−1.22	b
NGC 4020	0.15	1.50	0.55	2.23	0.13	−0.78	−3.05	−1.43	−2.55	−1.78	−2.09	−0.76	−0.73	−0.74	b
NGC 4051	0.42	7.55	0.38	6.96	0.18	0.34	−0.22	−0.80	−2.12	−0.51	−1.71	−0.83	−0.78	−0.74	d
NGC 4136	0.21	1.95	0.59	2.81	0.10	−0.07	−2.64	−2.19	−2.26	−1.82	−2.25	−0.37	−1.03	−1.14	b
NGC 4288	0.32	1.70	0.63	2.63	0.14	−1.04	−1.92	−2.47	−2.52	−1.82	−1.99	−0.44	−0.52	−0.05	b
NGC 4303	0.25	1.44	0.52	2.97	0.18	1.34	−0.17	0.10	−1.94	−0.03	−1.30	−0.96	−0.95	−1.20	c
NGC 4314	0.42	4.19	0.40	4.20	0.04	−0.21	−0.46	−0.84	−2.74	−0.80	−2.22	−1.67	−1.07	−1.76	c
NGC 4394	0.44	6.05	0.65	4.52	0.06	−0.15	−0.79	−1.19	−2.55	−0.72	−2.10	−1.29	−1.00	−1.53	d
NGC 4491	0.17	5.38	0.59	2.93	0.06	−1.69	−2.09	−2.16	−3.08	−1.15	−2.53	−1.50	−0.37	−1.50	d
NGC 4535	0.41	1.22	0.75	2.48	0.14	0.15	−0.78	−1.41	−3.36	−1.21	−3.06	−2.04	−1.39	−2.34	d
NGC 4548	0.45	1.70	0.31	3.83	0.07	−0.32	−1.67	−1.74	−2.69	−1.99	−2.48	−1.47	−1.92	−1.73	b
NGC 4569	0.08	3.07	0.42	3.86	0.09	0.32	−0.47	−0.00	−2.93	−1.13	−1.90	−1.54	−1.34	−1.30	b
NGC 4579	0.30	4.06	0.51	4.29	0.05	0.58	−0.21	−0.25	−2.59	−0.87	−1.97	−1.72	−1.50	−1.86	c
NGC 4580	0.14	1.31	0.42	2.53	0.06	−0.52	−1.83	−0.71	−2.52	−1.48	−1.64	−1.41	−1.07	−1.03	b
NGC 4647	0.22	2.50	0.32	2.98	0.33	0.37	−1.43	−1.13	−2.12	−0.83	−1.03	−0.99	−0.68	−0.81	b
NGC 4654	0.24	6.24	0.46	2.90	0.18	0.82	0.38	0.37	−1.92	0.70	−0.75	−0.66	0.87	−0.27	d
NGC 4725	0.34	1.60	0.56	3.96	0.09	0.52	−1.05	−0.70	−2.97	−2.19	−2.66	−1.69	−2.36	−2.04	b
NGC 5248	0.19	7.62	0.53	4.02	0.16	1.03	0.73	−0.13	−1.96	0.50	−1.22	−0.70	0.08	−1.00	d
NGC 5377	0.23	1.31	0.29	4.49	0.05	0.53	−1.20	−0.40	−2.28	−1.84	−2.43	−1.00	−1.92	−1.57	b
NGC 5457	0.21	2.64	0.68	2.82	0.22	0.44	−2.02	−1.44	−2.69	−0.54	−1.70	−0.81	−0.47	−1.05	c
NGC 5713	0.44	3.23	0.36	3.41	0.24	0.68	−0.15	0.09	−1.94	−0.59	−0.80	−1.04	−0.79	−0.80	b
NGC 5832	0.27	1.95	0.68	2.61	0.08	−1.53	−4.78	−2.00	−3.11	−3.10	−2.70	−0.90	−1.74	−1.00	a
NGC 6701	0.35	4.16	0.38	4.38	0.17	0.95	0.32	0.58	−1.68	−0.23	−0.94	−0.96	−0.86	−0.83	e
NGC 6946	0.35	2.85	0.56	2.98	0.26	0.72	−0.53	−0.30	−1.90	0.01	−1.12	−0.90	−0.60	−0.74	c
NGC 7080	0.36	4.16	0.39	4.67	0.14	0.79	0.08	0.04	−2.13	−0.58	−1.69	−1.16	−1.04	−1.17	c
NGC 7479	0.37	3.65	0.45	3.88	0.16	0.86	−0.08	0.18	−2.06	−0.38	−1.41	−0.97	−0.82	−1.00	c
NGC 7552	0.21	5.38	0.25	5.53	0.09	0.74	0.41	0.26	−1.68	0.42	−1.15	−0.92	−0.72	−0.89	d
NGC 7591	0.36	3.52	0.29	4.00	0.08	0.93	0.05	0.41	−2.05	−0.21	−1.16	−0.95	−0.95	−0.88	b
NGC 7741	0.44	2.53	0.49	2.73	0.18	−0.91	−2.26	−1.65	−2.50	−1.52	−1.84	−0.53	−0.29	−0.49	b
NGC 7798	0.19	5.04	0.54	3.53	0.14	0.82	−0.01	0.43	−1.18	0.27	−0.11	−0.32	−0.15	0.17	e
UGC 1249	0.27	2.15	0.72	2.61	0.18	−2.92	−4.00	−3.30	−3.38	−2.13	−2.60	−0.37	−0.00	−0.08	b

Notes. (1) Galaxy name. (2) Bar strength estimated using Equation (1). (3) and (4) The concentration and asymmetry index for the star formation distribution in one galaxy, described in Section 4.1. (5) and (6) The concentration and asymmetry index for the stellar mass distribution in one galaxy, described in Section 4.1. (7)–(15) The star formation rate, surface density of star formation rate, and specific star formation rate for the galaxy as an entirety, bulge and bar, respectively, calculated as in Section 4.2. (16) The stage in bar-driven evolutionary sequence, estimated from the position in Figure 9 and described in Section 5.2.

(Regan et al. 1995, 1999; Sheth et al. 2000; Zurita and Pérez 2008). In addition, simulations prove that the efficiency of driving gas depends on bar strength, i.e., stronger bars are able to transport more material at a faster rate than weak bars (e.g., Athanassoula 1992; Regan & Teuben 2004).

When focusing on different types of galaxies, we find that early-type galaxies have higher SFRs, but similar Σ_{SFR} and lower SSFRs compared with late-type galaxies. This may be due to the differing episodes of bar-driven gas inflow and star formation in galaxies with different types. In different episodes,
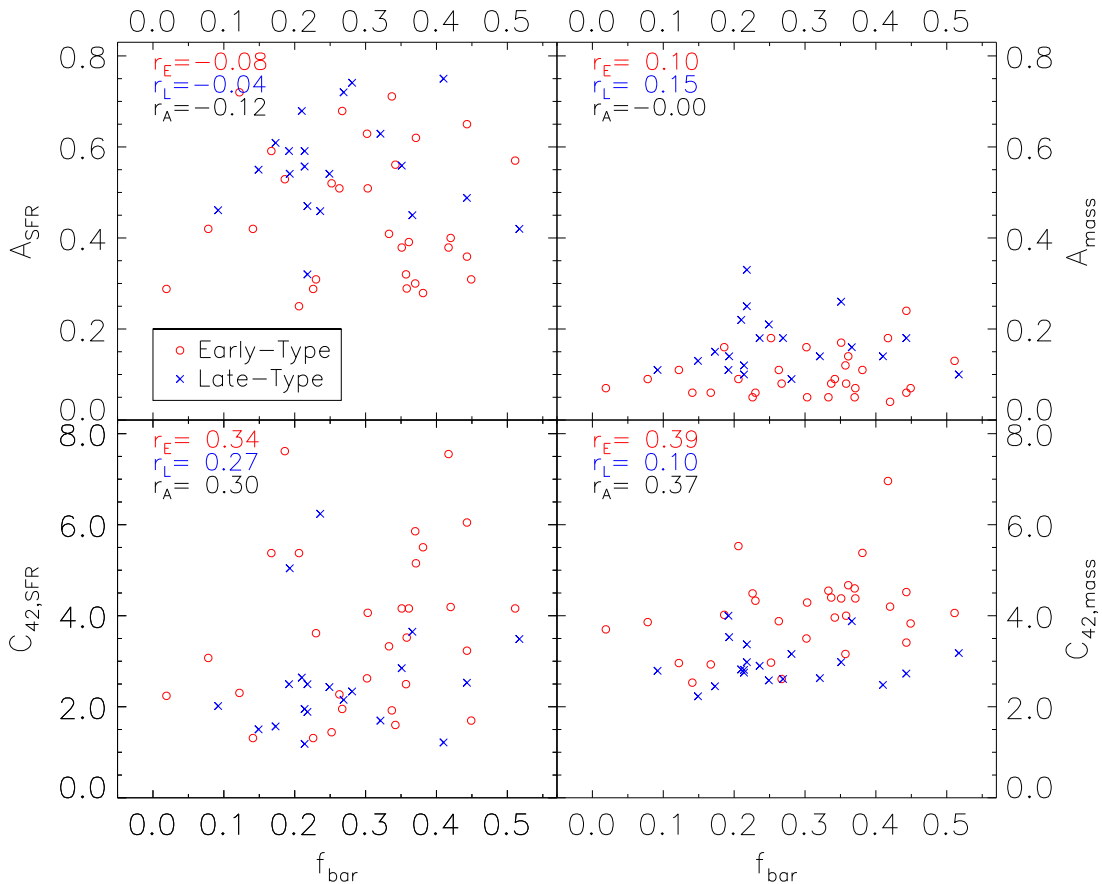
Figure 6. Relationship between bar strength and asymmetry (upper panels) and concentration index (lower panels) in our samples, derived based on the SFR images (left) and mass images (right) in Figure 1. In each panel, Spearman's rho tests are made to test the correlation between two variables, and the correlation coefficients are listed for the early-type galaxies (r_E), late-type galaxies (r_L), and the whole sample (r_A) of galaxies. The four panels use the same symbols: red circles for early-type galaxies and blue crosses for late-type ones.

there are likely differing bar stages, bulge mass, gas contents, and other physical conditions, all of which may contribute to this process (Coelho & Gadotti 2011; Ellison et al. 2011; Oh et al. 2012; Melvin et al. 2014). In late-type galaxies, stellar bars tend to be short, and bulges are usually small if they exist. This is likely the early stage of bar-driven evolution. In this episode, the effect of bars is not pronounced, although there is sufficient gas in galactic disks. Within the process, the gas is reserved in the bar and galactic central regions, and then star formation activity takes place there, resulting in the growth of the stellar bar and bulge along with a change in the galaxy morphology. Therefore, we can expect to find "mature" bars in early-type disks (Debattista et al. 2006; Giordano et al. 2011).

However, the various trends of star formation properties with bar strength suggest that another process is at play in reducing the bar effect: (1) massive bulges can dilute the bar nonaxisymmetric forces (Das et al. 2003; Laurikainen et al. 2004), thus some early-type spirals may have weaker bars than late-type systems (e.g., Laurikainen et al. 2002), (2) the amount of gas content may be not sufficient after being consumed by star formation in the previous process. Using CO observations, Sheth et al. (2005) found that six early-type barred spirals have very little molecular gas detected in bars and nuclear regions due to this gas being consumed during star formation. Therefore, early-type systems may have Σ_{SFR} in their bars and central regions that are similar to or lower than

those of late-type ones (Figure 7). Furthermore, these probabilities are likely the reasons why various star formation properties are associated with the intermediate-strength bars. Some of these bars may be transitioning from weak to strong and others with similar strength may have been weakened by massive bulges, although could have been strong once. Besides these factors, the difference between the timescales of bar evolution and star formation also can contribute to the complexity of the process (Roussel et al. 2001). It is likely that the lifetime of large-scale stellar bars is long enough to allow multiple episodes of central star formation, which can be used to interpret why some early-type bulges have lower SSFRs (Figure 7).

5.2. Bar-driven Secular Evolution

As mentioned above, bar-driven secular evolution is a complex process and is likely composed of a series of stages. There has been substantial progress in scenarios of secular evolution based on simulation evidence and observational results (e.g., Martin & Friedli 1997; Combes 2000; Bournaud & Combes 2002).

In the evolution process, numerous episodes of bar-driven gas inflow and star formation may take place, along with the growth, destruction, and re-formation of stellar bars (Combes 2009).
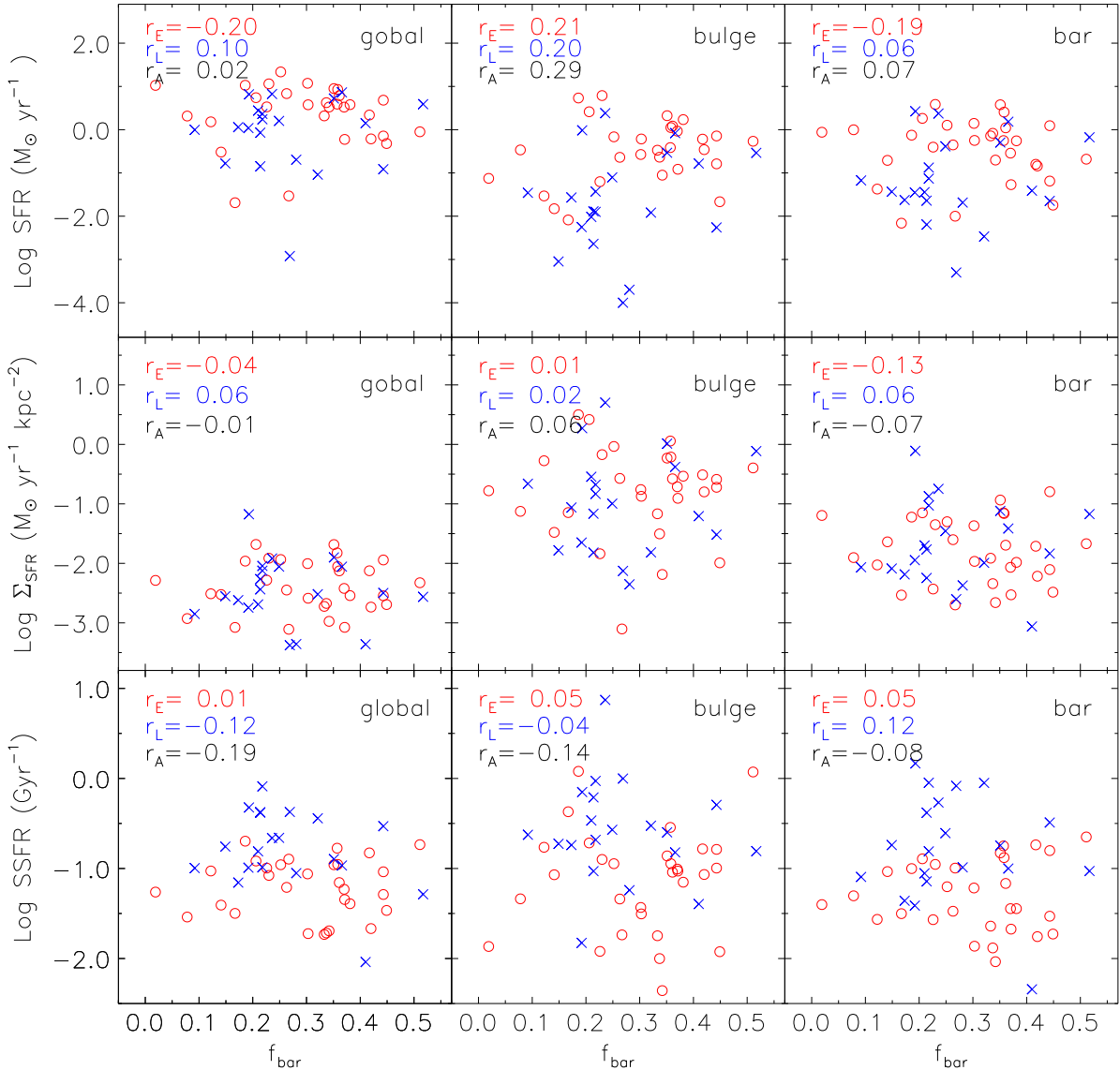
Figure 7. Relationship between bar strength and star formation activity in galaxies. From top to bottom, bar strength is compared with SFR, Σ_{SFR}, and SSFR in the global galaxy (left), the bulge (middle), and the bar (right), respectively. Spearman's rho tests are made as in Figure 6. The symbols are the same as in Figure 2.

In one simple scenario, various stages of evolution can also be divided based on the changing properties of star formation activity and gas content in galaxies. Using properties of Hα emission in barred galaxies, Verley et al. (2007) classified such galaxies into three main groups, in which Hα emission is mainly located in stellar bars, galactic central regions, and spiral arms. They suggested that these groups are different stages of an evolution process, similar to the trend proposed by Martin & Friedli (1997), but more detailed. Based on the properties of circumnuclear gas and star formation, Jogee et al. (2005) projected a possible picture of bar-driven dynamical evolution where the evolution process of barred galaxies was divided into three stages (i.e., Type I non-starburst, Type II nonstarburst, and circumnuclear starburst). In the three stages, large amounts of gas are transformed from stellar bars to galactic central regions step by step along with the star formation activity in bars and central regions. To complement this picture, Sheth et al. (2005) supplemented a post-starburst phase, i.e., Type III non-starburst, where the gas has been consumed by a circumnuclear starburst with no molecular gas in the bar region.

Given the above evolution pictures, molecular gas is transported from galactic disks to bulges through stellar bars, resulting in the rearrangement of material in the three galactic structures. Since star formation activity is correlated with the local gas density (Kennicutt 1998), the properties of star formation activity in bulges are likely associated with those in bars and disks. In addition, star formation activity in barred galaxies, especially in bulges, can change the galactic morphological properties (e.g., the asymmetry and concentration). To explore the correlations between them, we compared the star formation parameters of bulges, bars, and disks in our sample.

Figure 8 illustrates the correlations between the SFRs, Σ_{SFR}, and SSFRs in three galactic structures, along with the ratio lines from 10^{-2} to 10^2 plotted. We find that barred galaxies with more active star formation in bars tend to have more active star formation in bulges with a similar correlation between bars
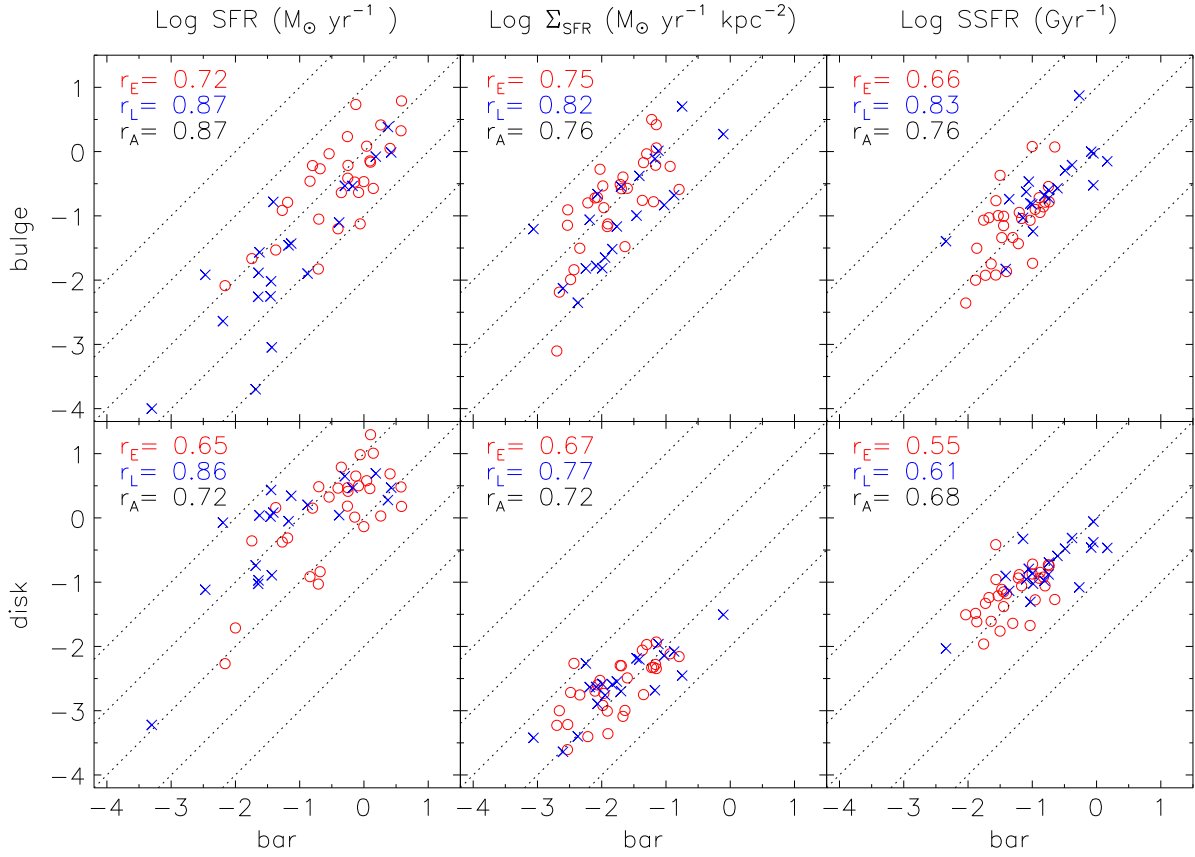
Figure 8. Comparison of the SFR (left), Σ_{SFR} (middle), and SSFR (right) in different structures: bar vs. bulge (top) and bar vs. disk (bottom). The dotted lines in each panel mark the scales between the two structures from 10^{-2} to 10^2, top to bottom, with steps of one order of magnitude. The symbols are the same as in Figure 2.

and disks. It is worth noting that most SFRs in bars are 0.1–10 times those in bulges, while the ratios of Σ_{SFR} in bars and bulges are in the range of 0.01–1, one magnitude lower than the SFR ratios. In addition, the SFR densities in disks are in general 0.01 times those in bulges. The enhanced star formation in bulges indicates the effect of bar-driven internal evolution, which can make the morphological properties vary with star formation activity in galaxies.

Combining the above evolution scenarios and observational results, we derive a possible criterion to quantify the different stages of an evolutionary sequence in Figure 9. In this figure, we use the concentration index of the global SFR in the galaxy, $C_{42,\mathrm{SFR}}$, and the ratio of Σ_{SFR} in the bulge and in the bar, $\frac{\Sigma_{\mathrm{SFR_{bulge}}}}{\Sigma_{\mathrm{SFR_{bar}}}}$, as the estimated parameters, and divide the parameter space into six fields (from a to f) as follows.

$$a: \frac{\Sigma_{\mathrm{SFR_{bulge}}}}{\Sigma_{\mathrm{SFR_{bar}}}} < 1, \ C_{42,\mathrm{SFR}} < 4.$$

This field is likely the early stage of bar-driven gas flow where a considerable fraction of the star formation activity is located in galactic outer disks, and bars have more active star formation than bulges. This stage is earlier than Type I non-starbursts in Jogee et al. (2005) because most gas is still in the outer disks.

$$b: 1 \leqslant \frac{\Sigma_{\mathrm{SFR_{bulge}}}}{\Sigma_{\mathrm{SFR_{bar}}}} < 10, \ C_{42,\mathrm{SFR}} < 4.$$

This is the second stage where the gas density in bulges is

higher than that in bars along with the gas inflow. Galaxies begin to have higher active star formation densities in bulges than those in bars, while the ratio is not larger than 10, and $C_{42,\mathrm{SFR}}$ is still lower than 4, indicating a non-negligible fraction of gas content is still in the disks.

$$c: 10 \leqslant \frac{\Sigma_{\mathrm{SFR_{bulge}}}}{\Sigma_{\mathrm{SFR_{bar}}}} < 10^{2-C_{42,\mathrm{SFR}}/8}$$

$$d: \frac{\Sigma_{\mathrm{SFR_{bulge}}}}{\Sigma_{\mathrm{SFR_{bar}}}} \geqslant 10^{2-C_{42,\mathrm{SFR}}/8}.$$

After most molecular gas has flowed into the galactic central regions, there are stages c and d. Field c is earlier in the process, corresponding to the later stage of Type II non-starbursts in Jogee et al. (2005), where galaxies either have a low SFR concentration $C_{42,\mathrm{SFR}}$ or have a ratio of SFR densities that is not high enough. Then as the intense star formation activity take place in bulges, galaxies in d may have most of their star formation activity concentrated in their central regions and may also consume most of gas there, similar to the stage of circumnuclear starbursts in Jogee et al. (2005).

$$e: 1 \leqslant \frac{\Sigma_{\mathrm{SFR_{bulge}}}}{\Sigma_{\mathrm{SFR_{bar}}}} < 10, \ C_{42,\mathrm{SFR}} \geqslant 4$$
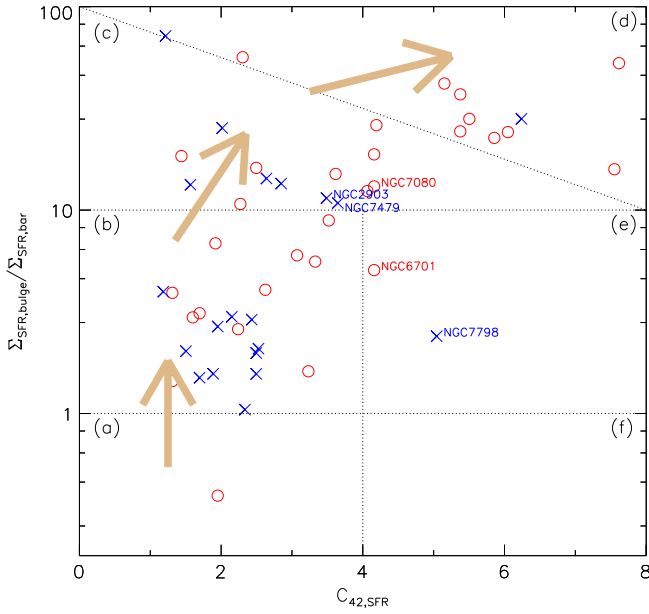
Figure 9. Comparison of the ratio of bulge-to-bar Σ_{SFR} with the concentration index of the SFR image. This plot is used as a criterion to quantify the different stages of a bar-driven evolutionary sequence (marked with arrows from *a* to *d*). See the text for details. The arrows show a possible sequence of evolution. Five galaxies are specially marked in the plot and they are mentioned in the text or studied in our previous works (Zhou et al. 2011, 2012). The symbols are the same as in Figure 2.

$$f: \frac{\Sigma_{SFR_{bulge}}}{\Sigma_{SFR_{bar}}} < 1,\ C_{42,SFR} \geqslant 4$$

e and *f* have $\frac{\Sigma_{SFR_{bulge}}}{\Sigma_{SFR_{bar}}}$ lower than 10 but $C_{42,SFR}$ larger than 4. There are very few galaxies located in the two fields. Given our assumption, galaxies with low $\frac{\Sigma_{SFR_{bulge}}}{\Sigma_{SFR_{bar}}}$ are probably in the stages before circumnuclear starbursts, where galaxies should have a low SFR concentration. However, if there are other factors at play (such as galaxy interactions), which can promote the process of bar-driven gas inflow, a large fraction of molecular gas can be concentrated in the bars and bulges of galaxies even when they are still in the early stage of a bar-driven process. For example, NGC 6701 (in Field *e*) is apparent because it is isolated, but it has been proven to produce interactions based on its morphological and kinematical features (Marquez et al. 1996). Similarly, NGC 7798 in Field *e* may also be in galaxy pairs and is affected by interactions (Chengalur et al. 1993). The resulting stages for our sample are listed in Table 4.

It is noted that our scenario just presents a rough criterion with uncertainties. For example, NGC 7479 is located in Stage *c* in this scenario, where it is suggested to be in the Type I non-starburst evolutionary phase under the effect of a minor merger (Paper I). As discussed in Section 5.1, bar-driven secular evolution is a complex process and many factors may contribute to it. To resolve this issue, more detailed observations and analysis of barred spirals are needed, along with statistical studies of large samples (e.g., using SDSS barred galaxies; F. Wang et al. 2014, in preparation).

6. SUMMARY

We present a study of bar-driven secular evolution from a sample of 50 nearby barred galaxies with weak and strong stellar bars. In this study, we characterize the bars using image decomposition, and estimate bar strength using the ellipticity-based parameter f_{bar}. Based on multi-wavelength photometry, we derive the properties of star formation activity in different stellar structures, and explore the correlations between these properties and stellar bars. The main results are as follows.

1. We use the image-fitting code BUDDA to perform a 2D decomposition of 3.6 μm images in the bar/bulge/disk components, and obtain the structural parameters of stellar bars. Most bars in our sample are detected within less than 9 kpc, and the bars in early-type spirals are in general longer in physical and normalized lengths and stronger in strength than those in late-type ones.

2. We calculate the rotational asymmetry A and concentration index C_{42} to quantify the distributions of star formation activity and stellar mass in galaxies. These parameters are compared with bar strength, but no clear trends are found. We find that early-type galaxies have a higher concentration index and lower asymmetry in both SFR and stellar mass distribution than late-type ones. Weak bars tend to be associated with low concentrical star formation activity, while strong bars appear to have a large scatter in the distribution of star formation activity.

3. We explore the correlations between bar strength and SFRs, Σ_{SFR}, and SSFRs in bulges and bars, as well as the global galaxies, while only weak positive trends are found between star formation activity in bulges and the bar strength along with large scatter. In addition, the early- and late-type galaxies have discernible differences in their SFRs and SSFRs, but have similar Σ_{SFR}.

4. Compared with previous studies, we suggest that the differing galaxy types, stellar mass distribution, and episodes of bar-driven gas inflow may contribute to the complexity of bar-driven secular evolution, which can be used to interpret why there are no visual trends between the parameters of star formation and bar strength.

5. We find evident correlations between the star formation activity in different galactic structures, i.e., barred galaxies with intense star formation in bars tend to have active star formation in their bulges and disks, indicating a bar-driven process in galaxies.

Finally, to quantify the different stages of the process, we derived a possible criterion using the ratio of Σ_{SFR} in the bulge and the bar, and the concentration index of the galactic global SFR as the estimated parameters. While uncertainties exist because of the contribution of other factors beside stellar bars, future work is needed to explore this issue.

REFERENCES

Abraham, R. G., & Merrifield, M. R. 2000, AJ, 120, 2385
Abraham, R. G., van den Bergh, S., & Nair, P. 2003, ApJ, 588, 218
Aguerri, J. A. L., Méndez-Abreu, J., & Corsini, E. M. 2009, A&A, 495, 491
Alonso-Herrero, A., & Knapen, J. H. 2001, AJ, 122, 1350
Athanassoula, E. 1992, MNRAS, 259, 345
Athanassoula, E. 2003, MNRAS, 341, 1179
Athanassoula, E., Gadotti, D. A., Carrasco, L., et al. 2009, RMxAA, 37, 79
Bershady, M. A., Jangren, A., & Conselice, C. J. 2000, AJ, 119, 2645
Bournaud, F., & Combes, F. 2002, A&A, 392, 83
Bundy, K., Ellis, R. S., Conselice, C. J., et al. 2006, ApJ, 651, 120
Buta, R., & Block, D. L. 2001, ApJ, 550, 243
Buta, R., Laurikainen, E., & Salo, H. 2004, AJ, 127, 279
Calzetti, D., Kennicutt, R. C., Engelbracht, C. W., et al. 2007, ApJ, 666, 870
Chengalur, J. N., Salpeter, E. E., & Terzian, Y. 1993, ApJ, 419, 30
Cheung, E., Athanassoula, E., Masters, K. L., et al. 2013, ApJ, 779, 162
Coelho, P., & Gadotti, D. A. 2011, ApJL, 743, L13
Combes, F. 2009, in ASP Conf. Ser. 419 Galaxy Evolution: Emerging Insights and Future Challenges, ed. S. Jogee, et al. (San Francisco, CA: ASP), 31
Combes, F. 2000, in ASP Conf. Ser. 197 Dynamics of Galaxies: from the Early universe to the Present, ed. G. A. Mamon, & V. Charmandaris (San Francisco, CA: ASP), 15
Conselice, C. J., Bershady, M. A., & Jangren, A. 2000, ApJ, 529, 886
Cowie, L. L., Songaila, A., Hu, E. M., & Cohen, J. G. 1996, AJ, 112, 839
Dale, D. A., Cohen, S. A., Johnson, L. C., et al. 2009, ApJ, 703, 517
Das, M., Teuben, P. J., Vogel, S. N., et al. 2003, ApJ, 582, 190
Debattista, V. P., Mayer, L., Carollo, C. M., et al. 2006, ApJ, 645, 209
de Souza, R. E., Gadotti, D. A., & dos Anjos, S. 2004, ApJS, 153, 411
de Vaucouleurs, G., de Vaucouleurs, A., Corwin, H. G., Jr, et al. 1991, in Third Reference Catalogue of Bright Galaxies RC3.9 C (New York: Springer)
Ellison, S. L., Nair, P., Patton, D. R., et al. 2011, MNRAS, 416, 2182
Erwin, P. 2005, MNRAS, 364, 283
Eskridge, P. B., Frogel, J. A., Pogge, R. W., et al. 2000, AJ, 119, 536
Fazio, G. G., Hora, J. L., Allen, L. E., et al. 2004, ApJS, 154, 10
Fisher, D. B. 2006, ApJ, 642, 17
Gadotti, D. A. 2008, MNRAS, 384, 420
Gadotti, D. A. 2011, MNRAS, 415, 3308
Gil de Paz, A., Boissier, S., Madore, B. F., et al. 2007, ApJS, 173, 185
Giordano, L., Tran, K. H., Moore, B., & Saintonge, A. 2011, arXiv:1111.1532
Hao, C.-N., Kennicutt, R. C., Johnson, B. D., et al. 2011, ApJ, 741, 124
Hancock, M., Smith, B. J., Struck, C., et al. 2007, AJ, 133, 676
Hawarden, T. G., Mountain, C. M., Leggett, S. K., & Puxley, P. J. 1986, MNRAS, 221, 41
Helou, G., Roussel, H., Appleton, P., et al. 2004, ApJS, 154, 253
Ho, L. C., Filippenko, A. V., & Sargent, W. L. W. 1997, ApJ, 487, 591
Hoopes, C. G., Walterbos, R. A. M., & Bothun, G. D. 2001, ApJ, 559, 878
Huang, J. H., Gu, Q. S., Su, H. J., et al. 1996, A&A, 313, 13
Isobe, T., & Feigelson, E. D. 1992, ApJS, 79, 197
James, P. A., Shane, N. S., Beckman, J. E., et al. 2004, A&A, 414, 23
Jogee, S., Barazza, F. D., Rix, H., et al. 2004, ApJ, 615, 105
Jogee, S., Scoville, N., & Kenney, J. D. P. 2005, ApJ, 630, 837

Kent, S. M. 1985, ApJS, 59, 115
Kennicutt, R. C. 1998, ARA&A, 36, 189
Kennicutt, R. C., Jr., Lee, J. C., Funes, S. J., et al. 2008, ApJS, 178, 247
Kennicutt, R. C., Hao, C.-N., Calzetti, D., et al. 2009, ApJ, 703, 1672
Kennicutt, R. C., Armus, L., Bendo, G., et al. 2003, PASP, 115, 928
Kim, T., Gadotti, D. A., Sheth, K., et al. 2014, ApJ, 782, 64
Knapen, J. H., Stedman, S., Bramich, D. M., Folkes, S. L., & Bradley, T. R. 2004, A&A, 426, 1135
Koopmann, R. A., Kenney, J. D. P., & Young, J. 2001, ApJS, 135, 125
Kormendy, J., & Fisher, D. B. 2005, RMxAA, 23, 101
Kormendy, J., & Kennicutt, R. C. 2004, ARA&A, 42, 603
Landolt, A. U. 1992, AJ, 104, 340
Laurikainen, E., Salo, H., & Buta, R. 2004, ApJ, 607, 103
Laurikainen, E., Salo, H., Buta, R., & Knapen, J. H. 2007, MNRAS, 381, 401
Laurikainen, E., Salo, H., & Rautiainen, P. 2002, MNRAS, 331, 880
Lee, J. C., et al. 2008, in ASP Conf. Ser. 396, Formation and Evolution of Galaxy Disks, ed. J. G., et al. (San Francisco, CA: ASP) 109
Li, H.-N., Wu, H., Cao, C., & Zhu, Y.-N. 2007, AJ, 134, 1315
Marquez, I., Moles, M., & Masegosa, J. 1996, A&A, 310, 401
Martin, P. 1995, AJ, 109, 2428
Martin, P., & Friedli, D. 1997, A&A, 326, 449
Meidt, S. E., Schinnerer, E., Knapen, J. H., et al. 2012, ApJ, 744, 17
Melvin, T., Masters, K., Lintott, C., et al. 2014, MNRAS, 438, 2882
Menéndez-Delmestre, K., Sheth, K., Schinnerer, E., Jarrett, et al. 2007, ApJ, 657, 790
Moustakas, J., & Kennicutt, R. C. 2006, ApJS, 164, 81
Muñoz-Mateos, J. C., Gil de Paz, A., Zamorano, J., et al. 2009, ApJ, 703, 1569
Oh, S., Oh, K., & Yi, S. K. 2012, ApJS, 198, 4
Pahre, M. A., Ashby, M. L. N., Fazio, G. G., & Willner, S. P. 2004a, ApJS, 154, 229
Pahre, M. A., Ashby, M. L. N., Fazio, G. G., & Willner, S. P. 2004b, ApJS, 154, 235
Piner, B. G., Stone, J. M., & Teuben, P. J. 1995, ApJ, 449, 508
Pompea, S. M., & Rieke, G. H. 1990, ApJ, 356, 416
Regan, M. W., & Teuben, P. J. 2004, ApJ, 600, 595
Regan, M. W., Sheth, K., & Vogel, S. N. 1999, ApJ, 526, 97
Regan, M. W., Vogel, S. N., & Teuben, P. J. 1995, ApJ, 449, 576
Rieke, G. H., Young, E. T., Engelbracht, C. W., et al. 2004, ApJS, 154, 25
Roussel, H., Sauvage, M., Vigroux, L., et al. 2001, A&A, 372, 406
Sakamoto, K., Okumura, S. K., Ishizuki, S., & Scoville, N. Z. 1999, ApJS, 124, 403
Salpeter, E. E. 1955, ApJ, 121, 161
Sanders, D. B., Mazzarella, J. M., Kim, D.-C., Surace, J. A., & Soifer, B. T 2003, AJ, 126, 1607
Sellwood, J. A., & Wilkinson, A. 1993, RPPh, 56, 173
Sérsic, J. L., & Pastoriza, M. 1965, PASP, 77, 287
Sheth, K., Regan, M. W., Vogel, S. N., & Teuben, P. J. 2000, ApJ, 532, 221
Sheth, K., Vogel, S. N., Regan, M. W., et al. 2002, AJ, 124, 2581
Sheth, K., Vogel, S. N., Regan, M. W., Thornley, M. D., & Teuben, P. J. 2005, ApJ, 632, 217
Sheth, K., Elmegreen, D. M., Elmegreen, B. G., et al. 2008, ApJ, 675, 1141
Sheth, K., Regan, M. W., Hinz, J., et al. 2010, PASP, 122, 1397
Smith, B. J., Struck, C., Hancock, M., et al. 2007, AJ, 133, 791
Verley, S., Combes, F., Verdes-Montenegro, L., Bergond, G., & Leon, S. 2007, A&A, 474, 43
Wang, J.-L. 2008, ChJAA, 8, 643
Wang, J., Kauffmann, G., Overzier, R., et al. 2012, MNRAS, 423, 3486
Werner, M. W., Roellig, T. L., Low, F. J., et al. 2004, ApJS, 154, 1
Whyte, L. F., Abraham, R. G., Merrifield, M. R., et al. 2002, MNRAS, 336, 128
Wu, H., Cao, C., Hao, C.-N., et al. 2005, ApJ, 632, 79
Wu, H., Zhu, Y. N., Cao, C., & Qin, B. 2007, ApJ, 668, 87
Zhou, Z.-M., Cao, C., Meng, X.-M., & Wu, H. 2011, AJ, 142, 38 (Paper I)
Zhou, Z.-M., Cao, C., & Wu, H. 2012, RAA, 12, 235 (Paper II)
Zhu, Y.-N., Wu, H., Cao, C., & Li, H.-N. 2008, ApJ, 686, 155
Zhu, Y.-N., Wu, H., Li, H.-N., & Cao, C. 2010, RAA, 10, 329
Zurita, A., & Pérez, I. 2008, A&A, 485, 5